Chemical Science

ROYAL SOCIETY OF CHEMISTRY

EDGE ARTICLE

View Article Online
View Journal | View Issue

Check for updates

Cite this: *Chem. Sci.*, 2025, **16**, 22580

All publication charges for this article have been paid for by the Royal Society of Chemistry

Enhanced red-light-driven hydrogen evolution by a diplatinum photocatalyst by the larger wavefunction leakage of iodide coordinated to the platinum center

Toma Kunikubo,[a] Raúl Castañeda,[b] Muralee Murugesu,[b] Jaclyn L. Brusso,[b] Kosei Yamauchi,[ac] Hironobu Ozawa *[a] and Ken Sakai *[a]

Received 23rd August 2025
Accepted 17th October 2025

DOI: 10.1039/d5sc06457k

rsc.li/chemical-science

The single-molecular photocatalyst $Pt_2(bpia)Cl_3$ (bpia = bis(2-pyridylimidoyl)amido), recently proven to promote red-light-driven hydrogen evolution reaction (HER) in water *via* singlet-to-triplet (S–T) transitions (*Angew. Chem. Int. Ed.*, 2025, **64**, e202418884), is shown to gain a significantly improved photocatalytic performance upon ligating iodide instead of chloride to give $Pt_2(bpia)I_3$. Upon iodide ligation, the absorption and emission energies both show a red shift basically due to destabilization of the HOMO by mixing of the iodide orbitals having essentially higher orbital energies compared to those of chloride. Consequently, the triplet lifetime and the luminescence quantum yield both decrease by obeying the energy gap law. The unique S–T transition features of $Pt_2(bpia)Cl_3$ are preserved in $Pt_2(bpia)I_3$ with the excited-state redox properties remaining unchanged. In spite of apparently disadvantageous photophysical features induced by the iodide ligation, $Pt_2(bpia)I_3$ is ascertained to promote the photocatalytic HER at a considerably higher rate in comparison with $Pt_2(bpia)Cl_3$, primarily attributed to the higher reductive quenching efficiency for the triplet excited state of $Pt_2(bpia)I_3$. The observations are rationalized due to the substantially more excellent acceptor characteristics of iodide, in which its larger wavefunction leakage significantly contributes to a larger electronic coupling factor in driving the outer-sphere electron transfer from the sacrificial electron donor.

Introduction

The photochemical hydrogen evolution reaction (HER) promoted by homogeneous and heterogeneous catalysts (Cat) has received considerable attention to solve the problems arising from the shortage of fossil fuels and global warming.[1] In the past several decades, extensive efforts have been made to achieve molecular-based artificial photosynthetic systems promoting the photocatalytic HER with high efficiency.[2] In our earlier studies, a photochemical system made up of EDTA (ethylenediaminetetraacetic acid disodium salt) as a sacrificial electron donor (SED), $[Ru(bpy)_3]^{2+}$ (bpy = 2,2′-bipyridine) as a photosensitizer (PS), and methylviologen (*i.e.*, MV^{2+}) as an electron relay was often adopted to evaluate the HER accelerated by various molecular Cat, such as mono- and dinuclear Pt(II) complexes,[3] tetracarboxylate Rh(II) dimers,[4] and N-heterocyclic carbene cobalt complexes.[5] As an extended approach, we and others also attempted to develop the dyads installed with a photosensitizing $[Ru(bpy)_2(phen)]^{2+}$ (phen = 1,10-phenantroline) chromophore and a catalytically active $Pt(bpy)Cl_2$ moiety (*i.e.*, $[RuPt]^{2+}$, Scheme 1a).[6,7] Through our investigations on a series of dyads with varying redox characteristics, we could gain an improved understanding of the mechanism of the photo-induced intramolecular electron transfer (ET) process from the PS moiety to the Cat moiety together with the mechanism of the HER by the Pt(II)-based molecular systems.[8]

On the other hand, we have reported that several $[PtCl(tpy)]^+$-type (tpy = 2,2′:6′,2″-terpyridine) complexes, such as [PtCl(tpy)]Cl,[9] $Na_2[PtCl(tctpy)]\cdot 5H_2O$[10] (tctpy = 2,2′:6′,2″-terpyridine-4,4′,4″-tricarboxylate), $[PtCl(Mepytpy)](ClO_4)_2\cdot H_2O$[11] (Mepytpy = 4′-(4-methyl-pyridinio)-2,2′:6′,2″-terpyridine), $[PtCl_2(bpyMV4)]^{8+}$,[12a] and $[PtCl_2(dpbpyMV4)]^{8+}$ (dpbpy = 4,4′-diphenyl-2,2′-bipyridine),[12c] shown in Scheme 1b–e, can serve as single-molecular photocatalysts for the HER in fully aqueous media in the presence of EDTA (abbreviated as H_2Na_2Y) as a SED. Our studies on these systems were mostly carried out in a weakly acidic aqueous pH 5.0 solution (0.1 M acetate buffer), in which the dianionic form of EDTA (*i.e.* H_2Y^{2-}) has the highest abundance in solution

---

[a] *Department of Chemistry, Faculty of Science, Kyushu University, Motooka 744, Nishi-ku, Fukuoka 819-0395, Japan. E-mail: h.ozawa@chem.kyushu-univ.jp; ksakai@chem.kyushu-univ.jp*

[b] *Department of Chemistry and Biomolecular Science, University of Ottawa, 10 Marie Curie, Ottawa, Ontario K1N 6N5, Canada*

[c] *Institute for Advanced Study, Kyushu University, Motooka 744, Nishi-ku, Fukuoka, 819-0395, Japan*

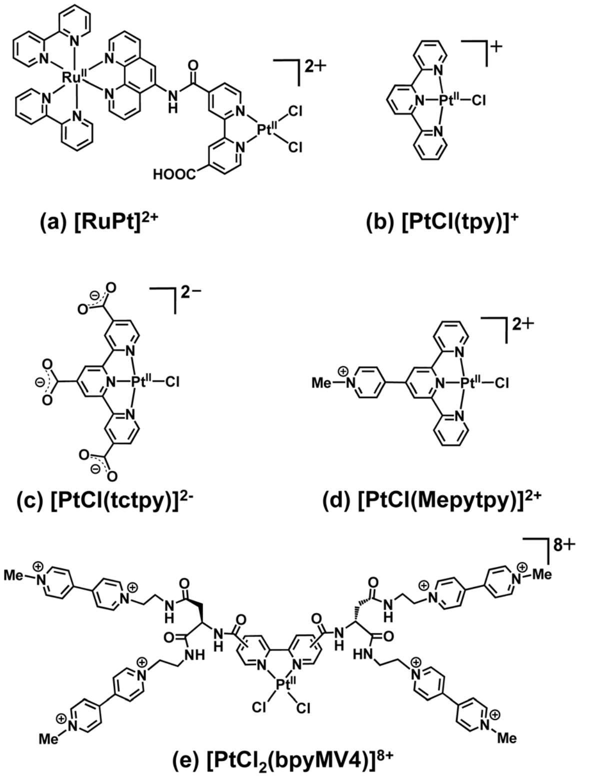

Scheme 1 Structures of (a) $[RuPt]^{2+}$,[6] (b) $[PtCl(tpy)]^{+}$,[9] (c) $[PtCl(tctpy)]^{2-}$,[10] (d) $[PtCl(Mepytpy)]^{2+}$,[11] and (e) $[PtCl_2(bpyMV4)]^{8+}$.[12a]

(93%) and plays a key role in promoting the intra-ion-pair ET during the reductive quenching (Scheme 2).[9] The transient absorption studies showed that such intra-ion-pair ET proceeds with time constants in the order of 10–100 ps after populating the ^{3}MLCT states.[8g,12c]

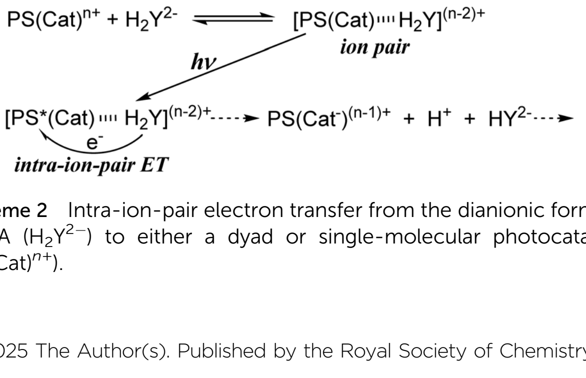

Scheme 2 Intra-ion-pair electron transfer from the dianionic form of EDTA (H_2Y^{2-}) to either a dyad or single-molecular photocatalyst ($PS(Cat)^{n+}$).

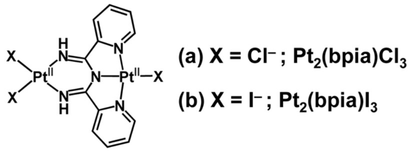

Scheme 3 Structures of (a) $Pt_2(bpia)Cl_3$,[14] and (b) $Pt_2(bpia)I_3$.

One of the major drawbacks in the above single-molecular photocatalysts lies in their limited light-harvesting capability with the ^{1}MLCT bands only absorbing light below 450 nm.[9–12] Single-molecular photocatalysts capable of harvesting the whole range of visible light are indeed quite limited. An important approach to this issue involves the reports by Turro *et al.*, in which paddlewheel-type dirhodium complexes were shown to serve as single-molecular photocatalysts promoting red-light-driven (*i.e.*, 670-nm-light-driven) HER in organic media in the presence of relatively strong acid and a SED.[13] Recently, we also demonstrated that a unique dinuclear Pt(II) complex ($Pt_2(bpia)Cl_3$,[14] bpia = bis(2-pyridylimidoyl)amido,[15] Scheme 3a) serves as a single-molecular photocatalyst for the HER with a superior light harvesting ability up to 650 nm.[14] In spite of its singlet-to-singlet transition absorption similarly located below 450 nm, $Pt_2(bpia)Cl_3$ was realized to be a rare example capable of harvesting light up to the red-light region due to the allowance of the singlet-to-triplet (*i.e.*, S–T) transitions.[14] In addition, $Pt_2(bpia)Cl_3$ shows an exceptionally long emission (105 ns) even in aqueous media at 20 °C.[14] Due to its superior photophysical properties, $Pt_2(bpia)Cl_3$ exhibits photocatalytic performance significantly higher than that of $[PtCl(tpy)]^{+}$-type single-molecular photocatalysts developed in our group.[14] More importantly, $Pt_2(bpia)Cl_3$ is the first example of a single-molecular photocatalyst promoting the low-energy-light-driven HER in water *via* direct S–T transitions ($\lambda > 580$ nm).[14] These results revealed the importance of raising the spin–orbit coupling constant derived from the diplatinum entity in order to allow the direct S–T transitions, as described elsewhere.[16] However, further optimization of a diplatinum-type single-molecular photocatalyst promoting the low-energy-light-driven HER in water still remains unexplored.

On the other hand, Rau and co-workers demonstrated that the $[RuPt]^{2+}$-type dyad (*i.e.*, $[Ru(tbbpy)_2(tpphz)PtX_2](PF_6)_2$, tbbpy = 4,4′-di-*tert*-butyl-2,2′-bipyridine, tpphz = tetrapyrido[3,2-*a*:2′,3′-*c*:3″,2″-*h*:2‴,3‴-*j*]phenazine; X = Cl$^-$ or I$^-$) exhibits visible-light-driven HER with much higher activity upon replacement of chloride by iodide, which was attributed to the increased electron density at the Pt center by the iodide ligation.[17] Inspired by the above report by Rau *et al.*, a new dinuclear Pt(II) complex $Pt_2(bpia)I_3$ (Scheme 3b) has been synthesized and examined by focusing on the role of iodide. To our surprise, upon replacement of chloride by iodide, the initial rate of H_2 evolution under visible-light irradiation ($\lambda > 400$ nm) becomes 4 times faster. Moreover, the amount of H_2 evolved under lower-energy light ($\lambda > 580$ nm) also becomes 7 times larger. Our study here revealed for the first time that excellent acceptor characteristics of iodide are crucial to significantly improve the photocatalytic performance of a diplatinum-type single-molecular photocatalyst due to its larger wavefunction leakage facilitating the reductive quenching of the triplet excited state by EDTA.

Results and discussion

$Pt_2(bpia)I_3$ was synthesized by the reaction of bis(2-pyridylimidoyl)amine (Hbpia)[15] and two equivalents of $PtI_2(cod)$[18] (cod = 1,5-cyclooctadiene) in DMF, and was obtained as a brown powder (Fig. S1). As reported for $Pt_2(bpia)Cl_3$,[14] $Pt_2(bpia)I_3$ only becomes well soluble when dissolved in a mixed solvent containing *N*-methyl-2-pyrrolidone (NMP). We therefore adopted a mixed solvent of either H_2O/NMP or DMF/NMP for all the experiments.

$Pt_2(bpia)I_3$ dissolved in a H_2O/NMP (9 : 1, v/v) mixture shows an absorption band at 409 nm (Fig. 1), revealing the overall shifts of the bands to the lower-energy region compared to those of $Pt_2(bpia)Cl_3$. Based on the TD-DFT results, the transition at 409 nm is predominantly assignable to the so-called metal/halide-to-ligand charge transfer (^{1}MX-LCT) transition from the diplatinum-centered (*i.e.*, *cis*-PtI_2-/PtI-centered) orbital (HOMO) to the π* orbital localized over the bpia (LUMO+1) (Fig. S2, S3 and Table S1). On the other hand, the transition in the lower-energy region (444 nm) is ascribed to the ^{1}MX-LCT transition from *cis*-PtI_2 to bpia (HOMO-1 → LUMO) and clearly shows a bathochromic shift relative to the transition of $Pt_2(bpia)Cl_3$ at 378 nm[14] (Fig. 1, S2, S3 and Table S1).

On the other hand, $Pt_2(bpia)I_3$ also displays a broad absorption band at around 530 nm, which can be viewed as related to the spectral features shown by $Pt_2(bpia)Cl_3$ (Fig. 1). We previously attributed this low-energy band to the spin-forbidden direct S–T transitions for $Pt_2(bpia)Cl_3$.[14] The TD-DFT results reveal that the low-energy band for $Pt_2(bpia)I_3$ is also assigned to the direct S–T transitions. In addition, the results further reveal that the transition energies together with the molar absorptivity ascribed to the S–T transitions are almost unaffected by the replacement of the halide ligands (Table S2), implying that iodide has a minor contribution to the spin–orbit coupling.

The concentration dependence of absorbance for $Pt_2(bpia)I_3$ reveals satisfaction of the Beer's law at all the maximum absorption wavelengths (350, 409, and 550 nm) at a concentration below 90 μM (Fig. S4), ruling out the presence of dimerization equilibrium in its ground state.

On the other hand, $Pt_2(bpia)I_3$ in a H_2O/NMP (9 : 1, v/v) mixture also exhibits weak luminescence at around 684 nm at 20 °C with a luminescence quantum yield of 0.2% (Fig. S5 and Table S3), slightly lower than the value of 0.3% reported for $Pt_2(bpia)Cl_3$.[14] The emission band is red-shifted by 39 nm compared to that of $Pt_2(bpia)Cl_3$ (645 nm).[14] The red shift observed in emission, together with that observed for the visible absorption (Fig. 1), can be rationalized by the cathodically shifted oxidation potential of the *cis*-PtX_2/PtX moieties in the iodide form compared to the chloride form as described below. The emission spectrum of $Pt_2(bpia)I_3$ upon excitation at 410 nm is almost consistent with that given by excitation at 500 or 585 nm (Fig. S6), confirming that all available excited states rapidly relax to the lowest-energy triplet state by satisfying Kasha's rule. On the other hand, the emission decay at 684 nm shows a good fit to a single exponential function, leading to an estimated emission lifetime of 20 ns (Table S4 and Fig. S7). This lifetime is only one fifth of that reported for $Pt_2(bpia)Cl_3$ (105 ns).[14] The emission quantum yield and lifetime are both diminished upon ligating iodide in place of chloride, which can be rationalized by the enhanced non-radiative decay rate due to the decrease in the HOMO–LUMO gap (*i.e.*, energy gap law). It must be noted here that almost all the Pt(II)-based single-molecular photocatalysts summarized in Scheme 1, except for $Pt_2(bpia)Cl_3$, are only emissive at 77 K but do not emit under such conditions due to the enhanced non-radiative deactivation.[19] The excited-state quenching of such non-emissive photocatalysts by the sacrificial electron donor EDTA has primarily been explained to proceed *via* static quenching within the ground-state adduct of photocatalysts with anionic EDTA.[11,12] In this regard, $Pt_2(bpia)X_3$ ($X = Cl^-$ or I^-) must be regarded as an exceptional family of photocatalysts affording a long-lived excited state, thus permitting the dynamic quenching under aqueous conditions. As described elsewhere, non-radiative decay rates are often greatly increased by the interactions of water molecules in aqueous media.[20]

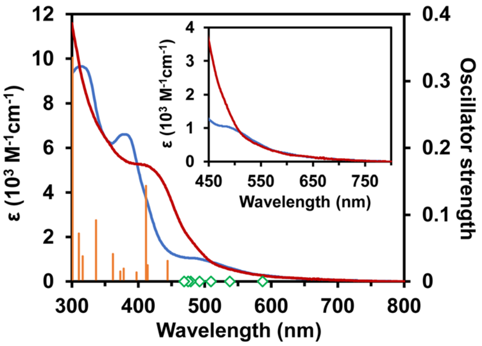

Fig. 1 Absorption spectra of $Pt_2(bpia)Cl_3$ (blue) and $Pt_2(bpia)I_3$ (red) in a mixed solvent of H_2O and NMP (9 : 1, v/v). Orange bars and green squares denote the oscillator strengths of S–S transitions and the calculated energies of S–T transitions, respectively. The inset shows the magnified figure.

$Pt_2(bpia)I_3$ in a DMF/NMP (4 : 1, v/v) mixture displays a broad oxidation peak above 0.7 V *vs.* SCE and a reversible reduction wave at −0.93 V *vs.* SCE with a peak-to-peak separation of 80 mV (Fig. S8–S10). The broad oxidation peak is assignable to the oxidation at the *cis*-PtI_2/PtI moiety as shown by the HOMO (Fig. S3). By analogy with our previous report on $Pt_2(bpia)Cl_3$,[14] the reversible reduction wave is reasonably assigned to the π*(bpia)-based one-electron reduction, as indicated by the LUMO, which is dominantly spread over the entire bpia in our DFT results (Fig. S2). This assignment is further ascertained by the DFT calculations for the one-electron-reduced species of $Pt_2(bpia)I_3$ (*i.e.*, $Pt_2(bpia^{-\bullet})I_3$), revealing that the spin density is indeed delocalized over the entire bpia moiety (Fig. S11a). Notably, the imine moiety of $Pt_2(bpia^{-\bullet})I_3$ exhibits a significant bend upon reduction (Fig. S11b), in contrast to the planar geometry stabilized for $Pt_2(bpia^{-\bullet})Cl_3$.[14]

On the other hand, the electrocatalytic activity of $Pt_2(bpia)I_3$ was evaluated in an aqueous acetate buffer (0.09 M, pH 5.0) containing NMP (9 : 1, v/v). The catalytic current for the HER starts to flow at around −1.05 V (Fig. 2). The overpotential for the HER ($\eta(E_{cat/2})$) catalyzed by $Pt_2(bpia)I_3$ is determined to be 680 mV from the potential difference between the potentials giving the half-height of the maximum catalytic current (−1.22 V, *i.e.*, $E_{cat/2}$) and the standard water reduction potential under these conditions (−0.54 V).[21] The $\eta(E_{cat/2})$ for $Pt_2(bpia)I_3$ is substantially larger than that of $Pt_2(bpia)Cl_3$ (420 mV,[14] Table S5), indicating that the driving force for the HER catalyzed by

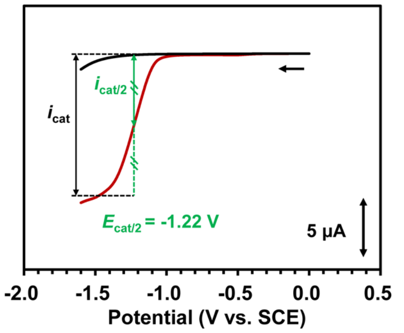

Fig. 2 LSVs of an aqueous acetate buffer solution (0.09 M, pH = 5.0) containing 10 vol% NMP in the presence (red) and absence (black) of 0.1 mM $Pt_2(bpia)I_3$. The scan rate for each measurement was 0.1 V s^{-1}. The diameter of the glassy carbon working electrode is 1 mm.

$Pt_2(bpia)I_3$ is larger than that of $Pt_2(bpia)Cl_3$. This is in line with the higher photocatalytic activity of $Pt_2(bpia)I_3$ compared to that of $Pt_2(bpia)Cl_3$, as shown below.

During 12 h of photolysis, $Pt_2(bpia)I_3$ evolves 10 μmol (1.1 mL) of H_2 from a 10 mL aqueous acetate buffer (0.09 M, pH 5.0) containing NMP (9 : 1, v/v) only in the presence of EDTA under visible light irradiation ($400 < \lambda < 800$ nm) (Fig. 3a), revealing that $Pt_2(bpia)I_3$ also serves as a diplatinum-type single-molecular photocatalyst. The TOF_{max} estimated for $Pt_2(bpia)I_3$ (4.4 h^{-1}, Table S6) is 4 times higher than that of $Pt_2(bpia)Cl_3$ (1.1 h^{-1},[14] Table S6), evidencing the rate-accelerating effect of iodide. As confirmed for $Pt_2(bpia)Cl_3$,[14] *in situ* dynamic light scattering measurements for the photolysis solution of $Pt_2(bpia)I_3$ were carried out to clearly rule out the formation of platinum nanoparticles during the initial 6 h of photolysis (Fig. S12 and S13), evidencing the homogeneous nature of catalysis by $Pt_2(bpia)I_3$. The reason for the higher activity of $Pt_2(bpia)I_3$ compared to $Pt_2(bpia)Cl_3$ can be discussed based on the following two key factors. One is the superior visible-light-harvesting ability of $Pt_2(bpia)I_3$ in the range of 400–500 nm. The other is the higher efficiency in the reductive quenching of $^{3*}Pt_2(bpia)I_3$ by EDTA, as discussed below. Thus, the obvious decrease in the rate of H_2 production for $Pt_2(bpia)I_3$ after 4 h of photolysis is likely due to the dissociation of iodide (Fig. 3a). However, our efforts to suppress the iodide dissociation by adding NaI failed due to the spontaneous reaction of NaI with NMP, leading to the formation of deep orange-colored species interfering with the photocatalysis (Fig. S14 and S15), as described elsewhere.[22] In the presence of 0.1 M NaI, the triplet emission is totally quenched (Fig. S16) and H_2 production is substantially suppressed (Fig. S17).

Even under the visible-light irradiation conditions ($\lambda > 500$ nm), $Pt_2(bpia)I_3$ also evolves 922 nmol of H_2 (Fig. 3b), proving that $Pt_2(bpia)I_3$ promotes the lower-energy-light-driven HER *via* the S–T transitions since only direct S–T transitions take place under these conditions (Fig. 1, Tables S1 and S2). To our surprise, $Pt_2(bpia)I_3$ also shows the photocatalytic activity for the HER higher than that of $Pt_2(bpia)Cl_3$ under photoirradiation above 500 nm even though the observed difference is not ascribable to the difference in their light-harvesting ability within this wavelength domain, as shown by their similarly leveled molar absorption coefficients (Fig. 1 and S18). Moreover, even under the red-light irradiation conditions ($\lambda > 580$ nm), $Pt_2(bpia)I_3$ evolves 134 nmol of H_2 over 6 h of photolysis (Fig. 3c), which is 7 times larger than H_2 evolution photocatalyzed by $Pt_2(bpia)Cl_3$. These results clearly indicate that $Pt_2(bpia)I_3$ is much superior to $Pt_2(bpia)Cl_3$ in promoting red-light-driven HER in water *via* the S–T transitions.

To better understand the behavior of $Pt_2(bpia)I_3$ during the photocatalysis, several additional experiments were performed as follows. First, emission quenching behavior was investigated at various EDTA concentrations (0–60 mM), revealing a decrease in emission intensity as the EDTA concentration increases (Fig. S19). The Stern–Volmer plot made by these results shows a linear correlation consistent with a dynamic quenching of the triplet ($^{3*}Pt_2(bpia)I_3$) by EDTA (Fig. 4a). By dividing the Stern–Volmer coefficient ($K_{SV} = 6.2$ M^{-1}) by the emission lifetime in the absence of a quencher ($\tau_0 = 20$ ns), the quenching rate constant can be determined as $k_q = 3.1 \times 10^8$ M^{-1} s^{-1}. It should be noted that the K_{SV} together with the k_q for $Pt_2(bpia)Cl_3$ were realized to be too small and could not be estimated.[14] In other words, $Pt_2(bpia)I_3$ has a substantially superior efficiency relative to $Pt_2(bpia)Cl_3$ in promoting the reductive quenching required for the photocatalytic HER. Nevertheless, the reduction potential of $^{3*}Pt_2(bpia)I_3$ (*ca.* 1.08 V), calculated from the

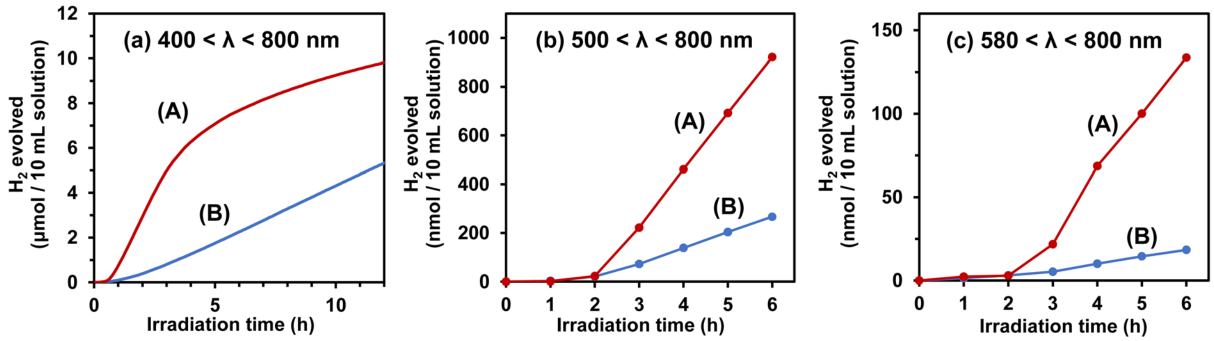

Fig. 3 Photocatalytic H_2 production from an aqueous acetate buffer solution (0.09 M, pH = 5.0) containing 10 vol% NMP and 30 mM EDTA in the presence of 0.05 mM $Pt_2(bpia)I_3$ (A) or 0.05 mM $Pt_2(bpia)Cl_3$ (B) under photoirradiation at $400 < \lambda < 800$ nm (a), $500 < \lambda < 800$ nm (b), and $580 < \lambda < 800$ nm (c). Photolysis solutions for (B) in all three measurements also contain 0.1 M NaCl to suppress the ligand replacement of chloride.

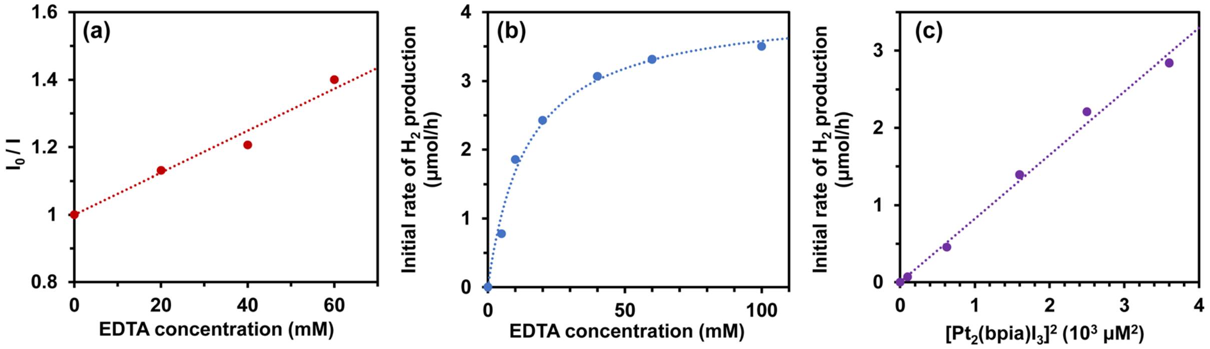

Fig. 4 (a) Stern–Volmer plot for the emission intensity of photolysis solution of $Pt_2(bpia)I_3$ against EDTA concentration. (b) Initial rate of H_2 production as a function of EDTA concentration, estimated from the amount of H_2 produced from the initial 30 to 60 min of photolysis under visible light irradiation ($400 < \lambda < 800$ nm). The calculated line (dotted line) is a least-squares fit to Michaelis–Menten equation. (c) Initial rate of H_2 production as a function of the square of $Pt_2(bpia)I_3$ concentration, estimated from the amount of H_2 produced from the initial 30 to 60 min of photolysis under visible light irradiation ($400 < \lambda < 800$ nm).

first reduction potential in water (−0.92 V, Table S7) and the E_{0-0} (*ca.* 2.0 eV, Fig. S20), is almost identical to that of $^{3*}Pt_2(bpia)Cl_3$ (*ca.* 1.05 V),[14] suggesting that the driving force for the quenching is not significantly different between them.

Next, the initial rate of H_2 evolution photocatalyzed by $Pt_2(bpia)I_3$ was investigated at various EDTA concentrations (0–100 mM), revealing clear saturation kinetics with the maximum rate of *ca.* 1.0 μmol h^{-1} (Fig. 4b and S21). In comparison, the initial rate of H_2 evolution by $Pt_2(bpia)Cl_3$ roughly exhibits saturation kinetics in the same EDTA concentration range with the maximum rate of only *ca.* 0.2 μmol h^{-1}.[14] Thus, these observations also indicate that $Pt_2(bpia)I_3$ shows a photocatalytic performance much higher than that of $Pt_2(bpia)Cl_3$ due to the higher efficiency in reductive quenching of $^{3*}Pt_2(bpia)I_3$ by EDTA. Note that our previous studies emphasized the importance of ion-pair adduct formation between the positively charged single-molecular photocatalysts and the divalent EDTA anion as shown in Scheme 2.[11,12] However, it is important to pay attention to the fact that $Pt_2(bpia)I_3$ does not rely on ion-pair formation with the dianionic form of EDTA under the photolysis conditions. Thus, the observed higher efficiency in reductive quenching of $^{3*}Pt_2(bpia)I_3$ can be correlated with the higher probability of ET between the EDTA donor and the acceptor orbitals of $^{3*}Pt_2(bpia)I_3$. The donor orbital is an amine donor of EDTA, while the acceptor site in the triplet can be computed by DFT. As depicted in Fig. 5a, the oxidized part at the ^{3}MX-LCT state can be recognized as the lower SOMO computed for $^{3*}Pt_2(bpia)I_3$, revealing that it is largely localized over the iodide singly coordinated to bis(pyridyl)amidoplatinum. In contrast, the SOMO of $^{3*}Pt_2(bpia)Cl_3$ consists of the dichlorodiimineplatinum- and bis(pyridyl)amidochloroplatinum-derived orbitals (Fig. 5b). More importantly, $^{3*}Pt_2(bpia)I_3$ shows a substantially larger spatial distribution at the accepting iodide orbital, indicative of the higher probability to accelerate the long-range ET (Fig. 5). As described elsewhere, the probability of ET between the donor (D) and acceptor (A) can be correlated with the relevant electronic coupling factor (H_{DA}).[23] Moreover, this factor is essentially governed by the degree of overlap between the donor and acceptor orbitals. In principle, the iodide has much larger wavefunction leakage relative to the chloride, and thus affords a larger H_{DA} resulting in higher reductive quenching efficiency in spite of bearing inferior excited-state properties. In our previous report on $Pt_2(bpia)Cl_3$,[14] the relatively slow H_2 evolution rate was primarily attributed to the lower probability of reductive quenching because the imine moieties, considered as the electron acceptor site in $^{3*}Pt_2(bpia)Cl_3$, are sterically blocked by the solvated NMP molecules.[14] In contrast, $^{3*}Pt_2(bpia)I_3$ possesses the spatially larger electron-accepting iodide orbital even if the imine moieties are similarly solvated by the NMP molecules (Fig. 5a), which rationalizes the higher probability of ET to promote the reductive quenching of $^{3*}Pt_2(bpia)I_3$ relative to $^{3*}Pt_2(bpia)Cl_3$.

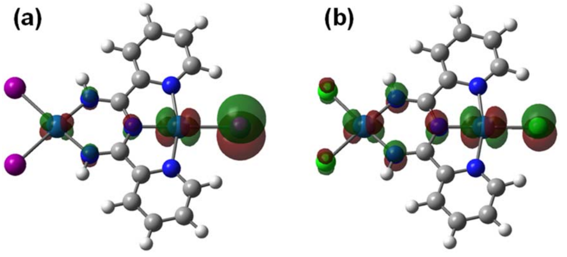

Fig. 5 Lower energy SOMO of $^{3*}Pt_2(bpia)I_3$ (a) and $^{3*}Pt_2(bpia)Cl_3$ (b).

Finally, the initial rate of H_2 evolution was further investigated at various $Pt_2(bpia)I_3$ concentrations (0–60 μM). The initial rate of H_2 evolution, estimated from the initial 2 h of photolysis, shows a second-order dependence on the $Pt_2(bpia)I_3$ concentration (Fig. 4c and S22), indicating that the H_2 evolution rate is limited by a step that is second order in either photocatalyst or photocatalyst-intermediate concentration. Nevertheless, dimerization of $Pt_2(bpia)I_3$ in its ground state is negligible because the absorbance change of $Pt_2(bpia)I_3$ completely obeys Beer's law at concentrations below 90 μM (Fig. S4). By analogy with the mechanism previously clarified for $Pt_2(bpia)Cl_3$,[14] the rate-limiting step can be regarded as a bimolecular coupling of $Pt_2(bpia^{-\bullet})I_3$ to yield H_2 and two equivalents of $Pt_2(bpia)I_3$.

Conclusions

In summary, we have successfully synthesized $Pt_2(bpia)I_3$ and characterized its photochemical and photophysical properties together with the photocatalytic activity for the HER from water with particular attention paid to its low-energy-light-harvesting ability. Upon replacing chloride with iodide, the absorption and emission energies both show red shifts basically due to the destabilization of the HOMO by the mixing of iodide orbitals which possess essentially higher orbital energies compared to those of chloride. The HOMO–LUMO gap thus exhibits a little shrinkage upon iodide ligation, leading to a lower luminescence quantum yield together with a shorter triplet lifetime by obeying the energy gap law. The unique S–T transition features of $Pt_2(bpia)Cl_3$ are preserved by $Pt_2(bpia)I_3$ without fundamental changes observed in the excited-state redox properties relevant to the photocatalytic HER. In spite of apparently disadvantageous photophysical features induced by the introduction of iodides, $Pt_2(bpia)I_3$ is ascertained to promote the photocatalytic HER at a considerably higher rate compared with $Pt_2(bpia)Cl_3$. This enhancement is rationally interpreted as due to the substantially more excellent acceptor characteristics of iodide based on the larger spatial distribution of the acceptor orbital participating in the outer-sphere ET from EDTA. Our study thus, for the first time, demonstrates an outstanding role of a heavier halide ion ligated to the catalytically active platinum center in order to have a substantially enhanced photoinduced ET rate in such photocatalytic reactions.

Experimental section

Materials

All solvents and reagents were of the highest quality available and were used as received. K_2PtCl_4 was purchased from TANAKA Kikinzoku Kogyo K. K. All other reagents were purchased from Tokyo Chemical Industry Co., Ltd, and were used as received. $Pt_2(bpia)Cl_3$,[14] Hbpia,[15] and $PtI_2(cod)$[18] were synthesized according to the literature methods. Purification of water was performed with an Advantec RFD250RB water distillation apparatus.

Synthesis of $[I_2Pt(bpia)PtI]\cdot 0.5NMP$ ($Pt_2(bpia)I_3$)

Hbpia (33 mg, 0.15 mmol) and $PtI_2(cod)$ (167 mg, 0.3 mmol) were dissolved in 4 mL dry DMF. The solution was stirred for 48 h at 110 °C followed by cooling it down to room temperature. The brown precipitate formed was collected by filtration, washed with chloroform (*ca.* 20 mL), acetone (*ca.* 20 mL), and diethyl ether (*ca.* 20 mL). Further purification was performed by recrystallization from a $Pt_2(bpia)I_3$-saturated NMP solution by adding excess acetone. Yield (brown powder): 15.1 mg, 10%. Anal. Calcd for $C_{14.5}H_{14.5}I_3N_{5.5}O_{0.5}Pt_2$ ($[I_2Pt(bpia)PtI]\cdot 0.5NMP$): H, 1.40; C, 16.67; N, 7.37. Found: H, 1.53; C, 16.76; N, 7.75. ESI-TOF mass (CH_3CN containing 5 vol% DMSO, positive mode) (*m*/*z*): 946.0 $[M-I^- + DMSO]^+$ ($[C_{14}H_{16}I_2N_5OPt_2S]^+$, calcd 946.0). The ^1H NMR spectrum could not be obtained due to the extremely low solubility in common organic solvents.

Measurements

^1H NMR spectra were acquired on a JEOL JNM-ESA 600 MHz spectrometer. ESI-TOF mass spectra were recorded on a JEOL JMS-T100LC mass spectrometer in positive ion mode. Infrared spectra were recorded on a PerkinElmer Spectrum One FT-IR spectrometer equipped with a Diamond ATR Crystal. UV-visible absorption spectra were recorded on a Shimadzu UV-3600 spectrophotometer, where all the sample solutions were thermostated at 20 °C. Transmittance spectra for two optical cutoff filters (Y-52 and R-60) were also recorded on a Shimadzu UV-3600 spectrophotometer. Luminescence spectra were recorded on a Shimadzu RF5300PC spectrofluorophotometer, equipped with a Hamamatsu R928 photomultiplier tube. Luminescence quantum yields were determined using a Hamamatsu C9920-02 absolute photoluminescence quantum yield measurement system equipped with a 150 W Xe lamp coupled to a monochromator and a Hamamatsu C10027-01 multichannel detector. Emission decays were recorded on a HORIBA FluoroCube 3000USKU, in which a diode laser (λ = 374 nm) (HORIBA N-470L) was used as the excitation source. Cyclic voltammograms (CVs) and square wave voltammograms (SWVs) were measured on a BAS ALS Model 602DKM electrochemical analyzer using a glassy carbon working electrode (Φ = 3 mm), a carbon rod counter electrode, and an Ag/Ag^+ reference electrode. The electrolyte solution was a mixed solvent of DMF and NMP (4 : 1, v/v) containing 0.1 M $TBAPF_6$ (tetra(*n*-butyl)ammonium hexafluorophosphate). The potentials were referenced relative to the internal ferrocene/ferrocenium couple (0.45 V *vs.* SCE in DMF).[24] Linear sweep voltammograms (LSVs) were measured on a BAS ALS Model 602DKM electrochemical analyzer using a glassy carbon working electrode (Φ = 1 mm), a carbon rod counter electrode, and a saturated calomel reference electrode (SCE). The electrolyte solution was an aqueous acetate buffer solution (0.09 M, pH = 5.0) containing 10 vol% NMP. All solutions used in these measurements were bubbled with Ar at least 20 min prior to the measurements. The pH values of the buffer solutions were measured by using a DKK-TOA HM-25R pH meter. Dynamic light scattering (DLS) experiments were carried out using an Otsuka Electronics ELSZ-2PS particle analyzer equipped with a diode laser (660 nm). Sample solutions used for the DLS measurements were filtered *via* a Whatman syringe filter (0.2 μm) twice to remove possible insoluble impurities and particles in solution before initiating each photolysis experiment.

Photocatalytic experiments

The photolysis solution (0.09 M acetate buffer solution (0.027 M CH_3COOH and 0.063 M CH_3COONa), pH = 5.0) contains 10 vol% NMP, 30 mM EDTA, and 0.05 mM $Pt_2(bpia)I_3$. Each photolysis solution was bubbled with Ar for 30 min before the photolysis experiment and kept at 20 °C during the photolysis. Photoirradiation was carried out using an ILC Technology

CERMAX LX-300 Xe lamp equipped with a CM-1 cold mirror ($400 < \lambda < 800$ nm, 300 W). The photolysis vial (21 mL) was immersed in a 20 °C water bath to remove IR radiation and to eliminate the temperature effects. The quantitative analysis of the H_2 evolved during the photocatalysis was carried out by using an automatic H_2 monitoring system developed by our group.[25] In this system, a continuous flow of Ar (10.0 mL min^{-1}, controlled by using an STEC SEC-E40/PAC-D2 digital mass flow controller) was bubbled through each photolysis solution (10 mL) contained in a Pyrex vial (*ca.* 20 mL). The vent gas from the vial was introduced into a 6-way valve, which allowed the automatic injection of the sample gas onto a gas chromatograph (Shimadzu GC-8A gas chromatograph equipped a Molecular Sieve 5A column of 2 m × 3 mm i.d. at 30 °C). The injection of sample gas was made by a control software operating on a Windows system. The signal output from the thermal conductivity detector was monitored by using a Shimadzu C-R8A integrator. Photocatalytic measurements under lower energy light irradiation conditions were conducted by using a Y-52 or R-60 cutoff filter (HOYA corporation), and the quantification of the amounts of H_2 evolved during the photocatalysis was manually performed by using a gastight syringe. The output signal from the thermal conductivity detector was recorded on a Shimadzu C-R8A integrator.

DFT calculations

Density functional theory (DFT) calculations were performed using the Gaussian 16 packages[26] to better understand the structural and spin-state candidates. The structures were fully optimized using the M06 hybrid functional[27] with the effect of solvation in water taken into consideration using the conductor-like polarizable continuum model (C-PCM) method.[28] The SDD basis set was adopted for the Cl, I and Pt atoms, while the 6-31+G* basis set was applied to the rest of atoms. Electronic excited states were calculated by the time dependent density functional theory (TD-DFT) calculation method as implemented in Gaussian 16 with the use of the same functional and basis sets described above.

Author contributions

T. K. performed the experiments, analyzed the data, and wrote the original draft. All the authors discussed the results and improved the manuscript.

Conflicts of interest

There are no conflicts to declare.

Data availability

The data supporting this article have been included as part of the Supplementary information (SI). Supplementary information: IR, absorption and emission spectra, DFT calculations, and results of electrochemical and photocatalytic measurements. See DOI: **https://doi.org/10.1039/d5sc06457k**.

Acknowledgements

This work was supported by JSPS KAKENHI grant numbers JP21H01952, JP22KK0074, JP23K04779, JP23H03831, JP24K01500, and JP24K01611. This work was also supported by JST PRESTO Grant Number JPMJPR22QA. H. O. acknowledges financial support from the ENEOS Tonengeneral Research/Development Encouragement & Scholarship Foundation and the Iketani Science and Technology Foundation. T. K. acknowledges financial support from the Kyushu University Q-PIT Support Program for Young Researchers and Doctoral Students, and JST SPRING, Japan Grant Number JPMJSP2136.

References

1 (*a*) A. J. Esswein and D. G. Nocera, *Chem. Rev.*, 2007, **107**, 4022–4047; (*b*) J. Barber, *Chem. Soc. Rev.*, 2009, **38**, 185–196; (*c*) K. E. Dalle, J. Warnan, J. J. Leung, B. Reuillard, I. S. Karmel and E. Reisner, *Chem. Rev.*, 2019, **119**, 2752–2875.

2 (*a*) K. Kalyanasundaram, J. Kiwi and M. Grätzel, *Helv. Chim. Acta*, 1978, **61**, 2720–2730; (*b*) M. Kirch, J. Lehn and J. Sauvage, *Helv. Chim. Acta*, 1979, **62**, 1345–1384; (*c*) C. V. Krishnan, B. S. Brunschwig, C. Creutz and N. Sutin, *J. Am. Chem. Soc.*, 1985, **107**, 2005–2015; (*d*) V. Artero, M. C. Kerlidou and M. Fontecave, *Angew. Chem. Int. Ed.*, 2011, **50**, 7238–7266; (*e*) H. Ozawa and K. Sakai, *AsiaChem.*, 2021, **2**, 80–87.

3 (*a*) K. Sakai and K. Matsumoto, *J. Mol. Catal.*, 1990, **62**, 1–14; (*b*) K. Sakai, Y. Kizaki, T. Tsubomura and K. Matsumoto, *J. Mol. Catal.*, 1993, **79**, 141–152; (*c*) K. Sakai and H. Ozawa, *Coord. Chem. Rev.*, 2007, **251**, 2753–2766; (*d*) K. Yamauchi, S. Masaoka and K. Sakai, *J. Am. Chem. Soc.*, 2009, **131**, 8404–8406.

4 S. Tanaka, S. Masaoka, K. Yamauchi, M. Annaka and K. Sakai, *Dalton Trans.*, 2010, **39**, 11218–11226.

5 (*a*) K. Kawano, K. Yamauchi and K. Sakai, *Chem. Commun.*, 2014, **50**, 9872–9875; (*b*) K. Yatsuzuka, K. Yamauchi, K. Kawano, H. Ozawa and K. Sakai, *Sustain. Energy Fuels*, 2021, **5**, 740–749; (*c*) K. Yamauchi, K. Kawano, K. Yatsuzuka, K. Kawamura, M. Kan and K. Sakai, *J. Am. Chem. Soc.*, 2025, **147**, 5602–5614.

6 H. Ozawa, M. Haga and K. Sakai, *J. Am. Chem. Soc.*, 2006, **128**, 4926–4927.

7 (*a*) S. Rau, B. Schäfer, D. Gleich, E. Anders, M. Rudolph, M. Friedrich, H. Görls, W. Henry and J. G. Vos, *Angew. Chem. Int. Ed.*, 2006, **45**, 6215–6218; (*b*) M. Elvington, J. Brown, S. M. Arachchige and K. J. Brewer, *J. Am. Chem. Soc.*, 2007, **129**, 10644–10645; (*c*) M. G. Pfeffer, B. Schäfer, G. Smolentsev, J. Uhlig, E. Nazarenko, J. Guthmuller, C. Kuhnt, M. Wächtler, B. Dietzek, V. Sundström and S. Rau, *Angew. Chem., Int. Ed.*, 2015, **54**, 5044–5048; (*d*) M. G. Pfeffer, C. Müller, E. T. E. Kastl, A. K. Mengele, B. Bagemihl, S. S. Fauth, J. Habermehl, L. Petermann, M. Wächtler, M. Schulz, D. Chartrand, F. Laverdière, P. Seeber, S. Kupfer, S. Gräfe, G. S. Hanan, J. G. Vos, B. Dietzek-Ivanšić and S. Rau, *Nat. Chem.*, 2022, **14**, 500–506.

8 (*a*) H. Ozawa, Y. Yokoyama, M. Haga and K. Sakai, *Dalton Trans.*, 2007, 1197–1206; (*b*) H. Ozawa and K. Sakai, *Chem. Lett.*, 2007, **36**, 920–921; (*c*) S. Masaoka, Y. Mukawa and K. Sakai, *Dalton Trans.*, 2010, **39**, 5868–5876; (*d*) H. Ozawa, M. Kobayashi, B. Balan, S. Masaoka and K. Sakai, *Chem.–Asian J.*, 2010, **5**, 1860–1869; (*e*) H. Ozawa and K. Sakai, *Chem. Commun.*, 2011, **47**, 2227–2242; (*f*) G. Ajayakumar, M. Kobayashi, S. Masaoka and K. Sakai, *Dalton Trans.*, 2011, **40**, 3955–3966; (*g*) C. V. Suneesh, B. Balan, H. Ozawa, Y. Nakamura, T. Katayama, M. Muramatsu, Y. Nagasawa, H. Miyasaka and K. Sakai, *Phys. Chem. Chem. Phys.*, 2014, **16**, 1607–1616; (*h*) M. Miyaji, K. Kitamoto, H. Ozawa and K. Sakai, *Eur. J. Inorg. Chem.*, 2017, **2017**, 1237–1244.

9 R. Okazaki, S. Masaoka and K. Sakai, *Dalton Trans.*, 2009, 6127–6133.

10 K. Yamauchi and K. Sakai, *Dalton Trans.*, 2015, **44**, 8685–8696.

11 (*a*) M. Kobayashi, S. Masaoka and K. Sakai, *Dalton Trans.*, 2012, **41**, 4903–4911; (*b*) M. Kobayashi, S. Masaoka and K. Sakai, *Angew. Chem. Int. Ed.*, 2012, **51**, 7431–7434.

12 (*a*) K. Kitamoto and K. Sakai, *Angew. Chem. Int. Ed.*, 2014, **53**, 4618–4622; (*b*) K. Yamamoto, K. Kitamoto, K. Yamauchi and K. Sakai, *Chem. Commun.*, 2015, **51**, 14516–14519; (*c*) K. Kitamoto and K. Sakai, *Chem. Commun.*, 2016, **52**, 1385–1388; (*d*) S. Lin, K. Kitamoto, H. Ozawa and K. Sakai, *Dalton Trans.*, 2016, **45**, 10643–10654; (*e*) K. Yatsuzuka, K. Yamauchi and K. Sakai, *Chem. Commun.*, 2021, **57**, 5183–5186.

13 (*a*) T. J. Whittemore, C. Xue, J. Huang, J. C. Gallucci and C. Turro, *Nat. Chem.*, 2020, **12**, 180–185; (*b*) J. Huang, J. C. Gallucci and C. Turro, *Chem. Sci.*, 2020, **11**, 9775–9783; (*c*) S. Lin and C. Turro, *Chem.–Eur. J.*, 2021, **27**, 5379–5387; (*d*) M. T. Fortunato, C. E. Moore and C. Turro, *J. Am. Chem. Soc.*, 2023, **145**, 27348–27357.

14 T. Kunikubo, R. Castañeda, M. Murugesu, J. L. Brusso, K. Yamauchi, H. Ozawa and K. Sakai, *Angew. Chem., Int. Ed.*, 2025, **64**, e202418884.

15 (*a*) R. Castañeda, A. Hollingshead, B. Gabidullin and J. L. Brusso, *Cryst. Growth Des.*, 2017, **17**, 6572–6578; (*b*) R. Castañeda, K. L. M. Harriman, J. W. L. Wong, B. Gabidullin, M. Murugesu and J. L. Brusso, *Eur. J. Inorg. Chem.*, 2019, **7**, 963–972; (*c*) A. A. Kitos, N. Mavragani, M. Murugesu and J. L. Brusso, *Mater. Adv.*, 2020, **1**, 2688–2706; (*d*) R. Castañeda, M. Rouzières, R. Clérac and J. L. Brusso, *J. Mater. Chem. C*, 2020, **8**, 4401–4407.

16 (*a*) P. Pander, A. V. Zaytsev, A. Sil, J. A. G. Williams, P.-H. Lanoë, V. N. Kozhevnikov and F. B. Dias, *J. Mater. Chem. C*, 2021, **9**, 10276–10287; (*b*) M. V. Kashina, K. V. Luzyanin, D. V. Dar'in, S. I. Bezzubov and M. A. Kinzhalov, *Inorg. Chem.*, 2024, **63**, 5315–5319.

17 M. G. Pfeffer, T. Kowacs, M. Wächtler, J. Guthmuller, B. Dietzek, J. G. Vos and S. Rau, *Angew. Chem., Int. Ed.*, 2015, **54**, 6627–6631.

18 A. Frei, S. Ramu, G. J. Lowe, H. Dinh, L. Semenec, A. G. Elliott, J. Zuegg, A. Deckers, N. Jung, S. Bräse, A. K. Cain and M. A. T. Blaskovich, *ChemMedChem*, 2021, **16**, 3165–3171.

19 D. K. Crites, C. T. Cunningham and D. R. McMillin, *Inorg. Chim. Acta*, 1998, **273**, 346–353.

20 F. Sueyoshi, X. Zhang, K. Yamauchi and K. Sakai, *Angew. Chem., Int. Ed.*, 2023, **62**, e202217807.

21 (*a*) J. A. S. Roberts and R. M. Bullock, *Inorg. Chem.*, 2013, **52**, 3823–3835; (*b*) A. M. Appel and M. L. Helm, *ACS Catal.*, 2014, **4**, 630–633.

22 (*a*) A. I. Frolov, R. N. Arif, M. Kolar, A. O. Romanova, M. V. Fedorov and A. G. Rozhin, *Chem. Sci.*, 2012, **3**, 541–548; (*b*) Z. Li, B. Ma, Y. Xu, Y. Lei, W. Lan, G. Wang, W. Li, Q. Wang, H.-L. Zhang and Z. Jin, *Adv. Funct. Mater.*, 2021, **31**, 2106380.

23 C. W. Kellett, W. B. Swords, M. D. Turlington, G. J. Meyer and C. P. Berlinguette, *Nat. Commun.*, 2018, **9**, 4916.

24 N. G. Connelly and W. E. Geiger, *Chem. Rev.*, 1996, **96**, 877–910.

25 M. Hirahara, S. Masaoka and K. Sakai, *Dalton Trans.*, 2011, **40**, 3967–3978.

26 M. J. Frisch, G. W. Trucks, H. B. Schlegel, G. E. Scuseria, M. A. Robb, J. R. Cheeseman, G. Scalmani, V. Barone, G. A. Petersson, H. Nakatsuji, X. Li, M. Caricato, A. V. Marenich, J. Blolino, B. G. Janesko, R. Gomperts, B. Mennucci, H. P. Hratchian, J. V. Ortiz, A. F. Izmaylov, J. L. Sonnenberg, D. Williams-Young, F. Ding, F. Lipparini, F. Egidi, J. Goings, B. Peng, A. Petrone, T. Henderson, D. Ranasinghe, V. G. Zakrzewski, J. Gao, N. Rega, G. Zheng, W. Liang, M. Hada, M. Ehara, K. Toyota, R. Fukuda, J. Hasegawa, M. Ishida, T. Nakajima, Y. Honda, O. Kitao, H. Nakai, T. Vreven, K. Throssell, J. A. Montgomery Jr., J. E. Peralta, F. Oligaro, M. J. Bearpark, J. J. Heyd, E. N. Brothers, K. N. Kudin, V. N. Staroverov, T. A. Keith, R. Kobayashi, J. Normand, K. Ragavachari, A. P. Rendell, J. C. Burant, S. S. Iyengar, J. Tomasi, M. Cossi, J. M. Millam, M. Klene, C. Adamo, R. Cammi, J. W. Ochterski, R. L. Martin, K. Morokuma, O. Farkas, J. B. Foresman and D. J. Fox, *Gaussian 16, revision C.01*, Gaussian, Inc., Wallingford, CT, 2016.

27 Y. Zhao and D. G. Truhlar, *Theor. Chem. Acc.*, 2008, **120**, 215–241.

28 (*a*) V. Barone and M. Cossi, *J. Phys. Chem. A*, 1998, **102**, 1995–2001; (*b*) M. Cossi, N. Rega, G. Scalmani and V. Barone, *J. Comput. Chem.*, 2003, **24**, 669–681.